Additive Manufacturing 124 (2026) 105213

Contents lists available at ScienceDirect

Additive Manufacturing

journal homepage: www.elsevier.com/locate/addma

Introducing a novel fabrication route for metastable β-type Ti–Cr–Sn alloys with ultra-high Sn content using pure elemental mixed powders via laser powder bed fusion

Naoki Nohira [a,*], Cheng Chen [a], Yilin Jin [a], Wan-Ting Chiu [a], Akira Umise [a], Takeshi Teramoto [d], Masaki Tahara [a,*], Ryosuke Ozasa [b,c], Takuya Ishimoto [b,c,e], Yuichiro Koizumi [b,c], Takayoshi Nakano [b,c], Hideki Hosoda [a]

[a] Institute of Integrated Research (IIR), Institute of Science Tokyo, 4259 Nagatsuta-cho, Midori-ku, Yokohama 226-8501, Japan
[b] Graduate School of Engineering, The University of Osaka, 2-1 Yamadaoka, Suita, Osaka 565-0871, Japan
[c] 3DPTec Integrated Center, Graduate School of Engineering, The University of Osaka, 2-1 Yamadaoka, Suita, Osaka 565-0871, Japan
[d] Department of Mechanical Engineering, Kobe University, 1-1 Rokkodai-cho, Nada-ku Kobe, 657-8501, Japan
[e] Titanium Research Center (TRC), University of Toyama, 3190 Gofuku, Toyama 930-8555, Japan

ARTICLE INFO

Keywords:
Additive manufacturing
β-Ti alloys
Laser powder bed fusion
Metastable
Ti–Cr–Sn

ABSTRACT

This study investigates the fabrication of ultra-high Sn-containing metastable β-type Ti–Cr–Sn alloys using Laser Powder Bed Fusion (L-PBF). By utilizing the rapid solidification inherent to L-PBF, retention of an ultra-high Sn metastable β phase at room temperature was achieved in compositions that are difficult to obtain via conventional processing routes. To address a key challenge in L-PBF, the high material cost associated with pre-alloyed powders, a mixture of pure elemental powders was employed as a cost-effective alternative feedstock. The effects of laser power on the microstructure, phase constitution, crystallographic texture, and mechanical properties of the as-built specimens were systematically evaluated. The results demonstrate that L-PBF successfully produced a homogeneous ultra-high Sn β solid solution while effectively suppressing the formation of ω phase and Ti_3Sn compounds. Under the highest laser power condition of 360 W, complete melting and the formation of a single β phase were achieved. The conventional unidirectional laser scanning strategy (X-scan), in which the scanning direction is kept constant between layers, resulted in $\langle 110 \rangle_\beta$ alignment along the build direction and $\langle 100 \rangle_\beta$ alignment along the scan direction. The specimen fabricated at 360 W exhibited the most homogeneous microstructure, together with appropriate strength, excellent ductility, and low Young's modulus. These findings demonstrate the feasibility of low-cost processing via L-PBF while achieving enhanced functional performance in high-Sn metastable β-Ti alloys.

1. Introduction

Metastable β-titanium alloys are attractive as biomaterials for stents, orthodontic applications, and prosthetic joint applications due to their high specific strength, high corrosion resistance, high biocompatibility, and functional properties such as low Young's modulus and shape memory effect (SME) [1,2]. Recently, we have succeeded in sufficiently suppressing the ω phase and achieving superelasticity at room temperature in Ti–Cr–Sn alloys with a high Sn addition, which is effective in suppressing the athermal ω, a problem in metastable β-Ti alloys [3]. However, the athermal ω has not been completely eliminated in these alloys [4]. Therefore, further addition of Sn should be attempted; however, the upper limit of Sn addition in Ti–Cr–Sn ternary alloys is about ~9 mol%Sn (~19.65 mass%Sn) [3–6].

Fig. 1 shows the phase diagrams of the Ti–Cr binary [7] and Ti–Sn binary [8] systems. In Ti–Cr–Sn alloys, the equilibrium phases at room temperature are α(Ti), $\alpha TiCr_2$, and Ti_3Sn, as expected from the Ti–Cr and Ti–Sn binary systems, and there is no β(Ti) phase. Therefore, to use these systems as metastable β-Ti alloys, the high-temperature phase (β phase) must be quenched into room temperature. Judging from the phase diagram (Fig. 1(b)), a single β phase can exist below 10.8 mol%Sn concentration at 1173 K.

---

[*] Corresponding authors.
E-mail addresses: nohira.n.aa@m.titech.ac.jp (N. Nohira), tahara.m.aa@m.titech.ac.jp (M. Tahara).

https://doi.org/10.1016/j.addma.2026.105213
Received 10 December 2025; Received in revised form 5 March 2026; Accepted 16 April 2026

Experimental [9] and calculated ternary phase diagrams [10] for the Ti–Cr–Sn ternary system report the equilibrium phases of Ti–10Cr–10Sn (mol%) at high temperatures. At 1173 K, the equilibrium phase was β(Ti) + αCr_2Ti + SnTi_3, and at 1373 K, β + SnTi_3. In the conventional melting process, solution treatment is carried out at about 1173–1273 K. The above results indicate that Ti_3Sn is formed at compositions above 10 mol%Sn, and a single β phase cannot be obtained by the conventional alloy fabrication methods.

Ti_3Sn is brittle [11] and leads to deviation of the β phase from the target composition. The formation of Ti_3Sn should be prevented to produce excellent β-Ti shape memory alloys (SMAs) as designed.

Recently, additive manufacturing (AM) has gained considerable interest as a novel fabrication process for various metal materials [12]. Among these processes, laser powder bed fusion (L-PBF) has shown great potential for fabricating β-Ti alloys [13]. It has been shown that the crystal orientation of β-Ti alloys can be controlled by appropriate process parameters of L-PBF [14,15], and this feature makes L-PBF a promising microstructure control process. Furthermore, L-PBF offers high cooling rates [16], which may enable the quenching of the metastable phases. The phase diagram indicates that a eutectic reaction L → β(Ti) + Ti_3Sn exists at 1847 K for Ti–15.9 mol%Sn [17]. In hypoeutectic compositions below this Sn content, β-Ti primary crystallizes during solidification. Accordingly, ideal rapid quenching from the liquid phase should result in a fully homogenized β-Ti solid solution without Ti_3Sn. Summarizing the above, the utilization of L-PBF is expected to be a new method for fabricating alloys with ultra-high Sn concentrations.

However, the L-PBF of Ti alloys faces difficulties in manufacturing due to the cost of pre-alloyed powders [18]. To overcome this drawback, some studies have been investigated fabricating alloys using a mixture of readily available pure elemental powders [19–22]. Although some incomplete melting has occurred in the case of elements such as Nb [20] and Mo [21], which have a high melting point relative to Ti, complete melting has been successfully achieved for Cr [22], which has a close melting point to Ti. Since Sn has a much lower melting point, Ti–Cr–Sn alloys without non-molten particles might be formed from pure metal mixed powders.

From the above considerations, the use of the AM process, even when employing a mixture of pure elemental powders for in-situ alloying, provides a unique opportunity to "freeze-in" the high-temperature β phase to room temperature, even in compositions where equilibrium processing inevitably results in β + Ti_3Sn formation.

Here, the significance of the present study can be summarized in two aspects:

(i) Fabrication of metastable β-Ti alloys with low Cr and ultra-high Sn compositions that are difficult to achieve by conventional routes; and
(ii) In-situ alloying of metastable β-Ti alloys using a mixture of pure elemental powders via L-PBF.

Therefore, a Sn-rich composition exceeding 10 mol% Sn in the low-Cr metastable β region was intentionally selected to test whether the rapid solidification inherent to L-PBF can extend the solubility limit of Sn in β-Ti beyond the conventional equilibrium boundary. Based on this compositional strategy, the influence of processing parameters on phase stability, texture evolution, and mechanical behavior was systematically investigated.

2. Materials and methods

2.1. Fabrication and sample preparation

The feedstock used in this study consisted of mixed powder particles of pure metals that form the constituents of the alloy. The Gas-atomized Titanium (Ti) powder (size distribution: 10–45 μm, purity: 99.7%) was supplied by OSAKA Titanium technologies (Amagasaki, Japan), Plasma-spheroidized Chromium (Cr) powder (size distribution: 15–53 μm, purity: 99.9%) was supplied by Advanced Engineering Materials (Changsha, China), and disk-atomized tin (Sn) powder (size distribution: 27–43 μm, purity: 99.9%) was supplied by Hikari Material Industry (Nagano, Japan). These pure elemental powders were mixed for 24 h using an agitator. The appearance of the mixed particles is shown in Fig. 2. Pure Ti, Cr, and Sn particles are shown in blue, green, and red, respectively. The particle shape is more clearly seen in the secondary electron image on the right. All particles appear to be almost spherical and dispersed. The measured particle size distributions (D_{10}, D_{50}, and D_{90}) are summarized in Table S1 and illustrated in Figure S1.

Rectangular specimens with a bottom dimension of 5 mm × 5 mm and a height of 9 mm were manufactured using an L-PBF system (EOS M 290, EOS, Krailling, Germany) in an Ar atmosphere.

Optimizing laser scanning parameters is crucial for achieving the desired microstructure and appropriate mechanical properties. A key factor in this optimization is the energy density (E, in J/mm^3). The energy density E [23,24] was calculated using the following Eq. (1):

$$E = P / vdt \tag{1}$$

where P is the laser power (W), v is the laser scan speed (mm/s), d is the hatch space (mm), and t is the thickness of a single layer (mm).

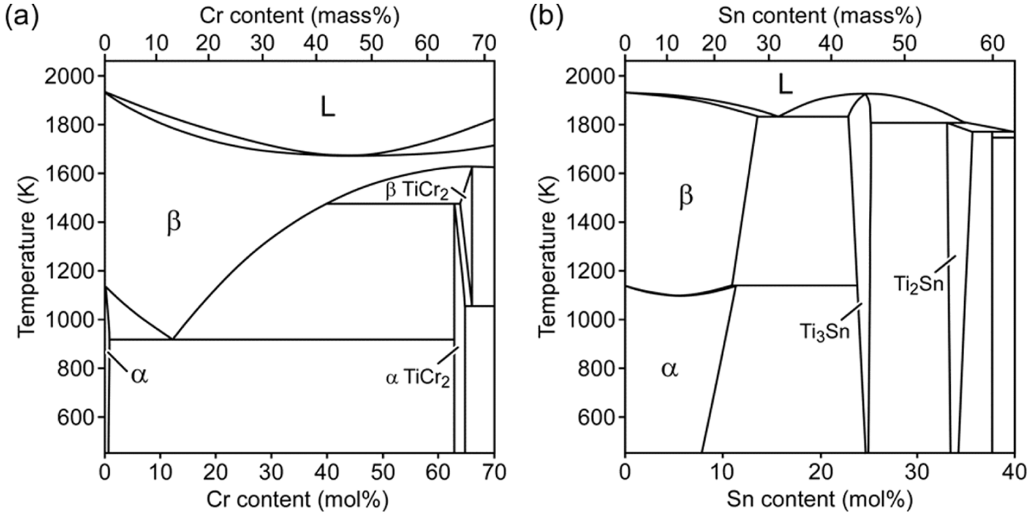

Fig. 1. The (a) Ti–Cr [7] and (b) Ti–Sn [8] binary phase diagrams.

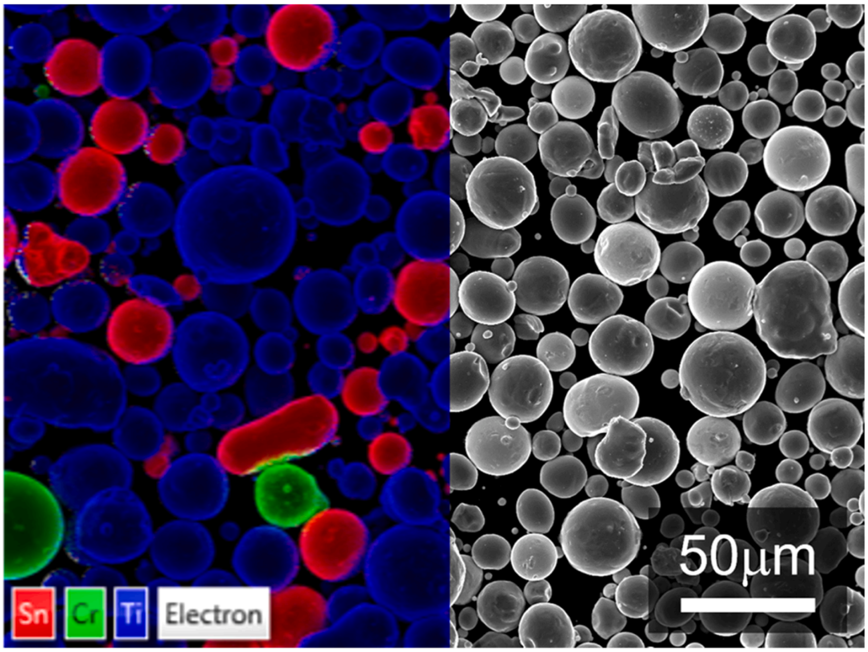

Fig. 2. Secondary electron image acquired by scanning electron microscopy and RGB elemental maps acquired by energy dispersive X-ray spectroscopy of the mixed particles. The elemental map (left) corresponds to the region adjacent to the area shown in the scanning electron micrograph (right), and is displayed by overlaying the RGB-colored mapping onto the corresponding micrograph.

In this study, the laser scan process parameters were set as follows: $v = 1200$ mm/s, $d = 0.08$ mm, $t = 0.06$ mm, and P was varied at 180, 240, 300, and 360 W. The resulting E was calculated as 31.25, 41.67, 52.08, and 62.50 J/mm^3, respectively. The samples will be identified and abbreviated hereafter based on their corresponding laser power P.

To investigate the elemental concentrations (Ti, Cr, Sn, and impurity Fe) before and after the L-PBF process, inductively coupled plasma atomic emission spectroscopy (ICP-AES) was performed on both the mixed powder and the as-built specimen (fabricated at 360 W). Oxygen concentrations were also measured by the inert gas fusion method.

To prepare samples for each evaluation, as-built specimens were cut by electrical discharge machining (EDM). The specimen surfaces were lapped with emery papers and then polished with colloidal silica to achieve a smooth finish. Microstructure characterization in the subsequent analysis was specifically conducted on the XY plane of the specimens.

2.2. *Characterizations*

Phase constituents of the alloys were identified by using an X-ray diffractometer (XRD; X'Pert-PRO-MPD, Malvern PANalytical, Malvern, UK) at room temperature (RT; 295 K). The scanning range spanned from 20° to 120° by using CuK$_\alpha$ radiation. A standard silicon plate was used as a reference for correcting external errors.

A scanning electron microscope (SEM; S-4300SE, Hitachi, Tokyo, Japan) coupled with energy-dispersive X-ray spectroscopy (EDS; EMAX ENERGY, Horiba, Kyoto, Japan) was used for the quantitative analysis of chemical composition and homogeneity. A SEM (SU5000, Hitachi, Tokyo, Japan) equipped with an electron backscattered diffraction (EBSD; EDAX detector with OIM software package, Ametek, Berwyn, US) was used for the microstructural observations. Prior to these SEM observations, specimens were electropolished to achieve a fine surface finish. The electrolyte for electropolishing was composed of methanol, butanol, and perchloric acid, mixed in a ratio of 10:6:1, respectively. The electropolishing was performed at a temperature of 233 K.

The texture was evaluated using X-ray pole figures (XPFs) of $\{110\}_\beta$, $\{200\}_\beta$, $\{211\}_\beta$, $\{220\}_\beta$, and $\{310\}_\beta$ poles measured with XRD system (X'pert PRO-MRD, Malvern PANalytical, Malvern, UK) at RT, using the Schulz reflection technique [25] and CuK$_\alpha$ radiation. The tilt angle ranges from 0 to 75°. Based on these XPFs, the Orientation Distribution Functions (ODFs) were calculated by the WIMV method [26].

The internal microstructure of the homogeneous specimen ($P = 360$ W) was observed with a transmission electron microscope (TEM; JEM2100, JEOL, Tokyo, Japan). The specimens for TEM were fabricated using a focused ion beam (FIB) (JIB-4500, JEOL, Tokyo, Japan).

2.3. *Mechanical testing*

Compression tests were performed in the x-direction (laser scan direction) to assess the mechanical properties of the as-built specimens using an Instron-type universal testing machine (Autograph AG–X plus 20 kN, SHIMADZU, Kyoto, Japan). The compression specimens had nominal dimensions of 2 mm × 2 mm × 5 mm. The specimen surfaces were mechanically polished to obtain a rectangular shape prior to testing. The tests were conducted at RT with a strain rate of 5.0×10^{-4} s^{-1}, starting with nine loading–unloading cycles, each cycle applying a 1% strain increment to assess deformation behaviors, including shape memory and superelasticity. Following these cycles, the specimens were subjected to continuous loading until fracture.

In order to ensure a reliable evaluation of Young's modulus, additional experiments were performed using a direct optical strain measurement method. The specimen side surface was coated with a black spray and white speckles to create tracking markers. During compression testing, the specimen surface was recorded using a high-resolution digital camera system.

The displacement between selected marker pairs was analyzed frame by frame using digital image analysis software (DIPP-Motion V, DITECT Corporation, Tokyo, Japan) to obtain the true specimen strain. The applied stress was calculated from the load recorded by the testing machine and synchronized with the optical data. Young's modulus was determined from the linear region of the stress–strain curve using data between 0.5 $\sigma_{\max}$ and 0.95 $\sigma_{\max}$, where $\sigma_{\max}$ denotes the maximum stress in each loading segment.

For statistical reliability, three loading–unloading cycles were analyzed per specimen, and five independent marker pairs were tracked in each cycle, resulting in 30 modulus values per specimen in total. The averaged value was adopted as the experimental Young's modulus.

2.4. *Ab-initio calculation of β phase*

The elastic constants of the β phase were evaluated by ab-initio simulations. Density functional theory simulations were performed with the Vienna Ab-initio Simulation Package (VASP) [27–30] using the projector augmented wave method (PAW) [31,32] and the generalized gradient approximation proposed by Perdew, Burke, and Ernzerhof (GGA-PBE) [33]. The plane wave cutoff energy was 400 eV, and the energy convergence criterion in the electron self-consistent loop was 10^{-6} eV. Internal atomic positions were relaxed until the residual forces became less than 10^{-2} eV/angstrom. The special quasi-random structure (SQS) method [34] was employed to represent the random structure of the β phase. The SQS cell was obtained by ATAT code [35]. The generated SQS cell consists of 54 atoms (46 Ti atoms, 6 Sn atoms, and 2 Cr atoms), which is a threefold enlargement of the bcc unit cell along the principal axis. The lattice constants (327.4 pm) obtained experimentally at RT are adopted to predict the elastic constants at RT. The Brillouin zone was sampled employing Monkhorst-Pack k-point meshes with a 5 × 5 × 5 grid for the SQS cell lattice.

2.5. *Calculation method of elastic constants*

Following the construction of the SQS supercell described above, the elastic constants were evaluated using the strain energy method [36]. The elastic constants correspond to the second derivatives of the total energy with respect to strain and are expressed as second-order coefficients of the strain–energy relationship. After full structural relaxation, small symmetry-preserving strains within the linear elastic regime were applied to the optimized supercell, and the total energy was calculated for each strain state.

For an ideal cubic BCC crystal, there are three independent elastic constants, C_{11}, C_{12}, and C_{44}. However, the difference in atomic species in the SQS cell reduces the crystal symmetry and results in slight variations among nominally equivalent elastic components. To account for these variations, the averaged values $\overline{C}_{11}$, $\overline{C}_{12}$, and $\overline{C}_{44}$ were adopted as the representative values in this study.

$$\overline{C}_{11} = \frac{C_{11} + C_{22} + C_{33}}{3}$$

$$\overline{C}_{12} = \frac{C_{12} + C_{23} + C_{13}}{3}$$

$$\overline{C}_{44} = \frac{C_{44} + C_{55} + C_{66}}{3} \tag{2}$$

The strain matrices applied to the calculations of the elastic constants are summarized in Table 1. Strain energy curves were obtained by applying ±0.01 and ±0.005 to δ .

3. Results and discussion

Table 2 shows the composition of the mixed metal powder before the AM building process and the composition of the as-built specimen (360 W). The unavoidable Fe impurities in the metal powder were 0.02 mol% and 0.03 mol% before and after L-PBF fabrication, respectively. Since the Fe contamination was trace amounts and no significant change was observed, its effect is neglected hereafter. The overall composition before fabrication was Ti–3.45Cr–10.33Sn–0.28 O, and after AM, it was Ti–3.29Cr–10.89Sn–0.34 O. The change in Cr content was −0.16 mol%, Sn was + 0.56 mol%, and O was + 0.06 mol%.

The nominal powder composition based on the mixing ratio and the measured composition of the as-built specimen are plotted on the Ti–Cr–Sn ternary diagram in Fig. 3. The comparison between the mixed particles and the as-built composition reveals a measurable deviation during the L-PBF process, reflecting compositional redistribution during melting and solidification. As shown in the ternary phase map, the present compositions are located beyond the β / β+Ti_3Sn boundary in the 1173 K phase diagram [10], where conventional equilibrium processing would be expected to result in a β+Ti_3Sn two-phase constitution. Therefore, if a single β phase is obtained under L-PBF conditions, it would represent a metastable ultra-high Sn β alloy beyond the conventional equilibrium boundary.

The compositions of the samples prepared by the L-PBF deviated slightly from those of the powder mixtures. In terms of boiling point and vapor pressure, there was concern that Sn would decrease more than Cr, but in fact, only a slight decrease in Cr was observed. Vaporization losses in AM are often a problem, and various studies have been summarized [37], but it is known that it is difficult to discuss merely from vapor pressure [37]. After alloying, the activity coefficient may also be a dominant factor [38]. The inconsistency in the present study with the trends of easily understandable indices such as vapor pressure was consistent with reports [38] that Cr is the most prominent among Ti, Cr, and Sn reported in vaporization in PBF processes.

Deviation from the target composition by L-PBF affects various physical properties. In Ni–Ti alloys, typical shape memory alloys, it has been reported that the transformation temperature changes with compositional variations due to the L-PBF process [39]. In this case, the importance of designing compositions that include the amount of Ni losses during melting was pointed out [40].

Table 2
Elemental composition of Ti–Cr–Sn alloy before and after L-PBF.

(mol%)	**Cr***	**Sn***	**Fe***	**O****	**Ti***
mixed powders	3.45	10.33	0.02	0.28	85.92
as-built specimen ($P = 360$W)	3.29	10.89	0.03	0.34	85.45
(mass%)	**Cr***	**Sn***	**Fe***	**O****	**Ti***
mixed powders	3.25	22.20	0.02	0.08	74.45
as-built specimen ($P = 360$W)	3.08	23.25	0.03	0.10	73.54

* Inductively coupled plasma atomic emission spectroscopy,
** Inert gas fusion method

Table 1
Strain matrices for elastic constants calculations.

$C_{11}: \begin{pmatrix} 1+\delta & 0 & 0 \\ 0 & 1 & 0 \\ 0 & 0 & 1 \end{pmatrix}$	$C_{11}\ C_{12}\ C_{22}: \begin{pmatrix} 1+\delta & 0 & 0 \\ 0 & 1+\delta & 0 \\ 0 & 0 & 1 \end{pmatrix}$	$C_{44}: \begin{pmatrix} 1 & 0 & 0 \\ 0 & 1 & 0.5\delta \\ 0 & 0.5\delta & 1 \end{pmatrix}$
$C_{22}: \begin{pmatrix} 1 & 0 & 0 \\ 0 & 1+\delta & 0 \\ 0 & 0 & 1 \end{pmatrix}$	$C_{22}\ C_{23}\ C_{33}: \begin{pmatrix} 1 & 0 & 0 \\ 0 & 1+\delta & 0 \\ 0 & 0 & 1+\delta \end{pmatrix}$	$C_{55}: \begin{pmatrix} 1 & 0 & 0.5\delta \\ 0 & 1 & 0 \\ 0.5\delta & 0 & 1 \end{pmatrix}$
$C_{33}: \begin{pmatrix} 1 & 0 & 0 \\ 0 & 1 & 0 \\ 0 & 0 & 1+\delta \end{pmatrix}$	$C_{11}\ C_{13}\ C_{33}: \begin{pmatrix} 1+\delta & 0 & 0 \\ 0 & 1 & 0 \\ 0 & 0 & 1+\delta \end{pmatrix}$	$C_{66}: \begin{pmatrix} 1 & 0.5\delta & 0 \\ 0.5\delta & 1 & 0 \\ 0 & 0 & 1 \end{pmatrix}$

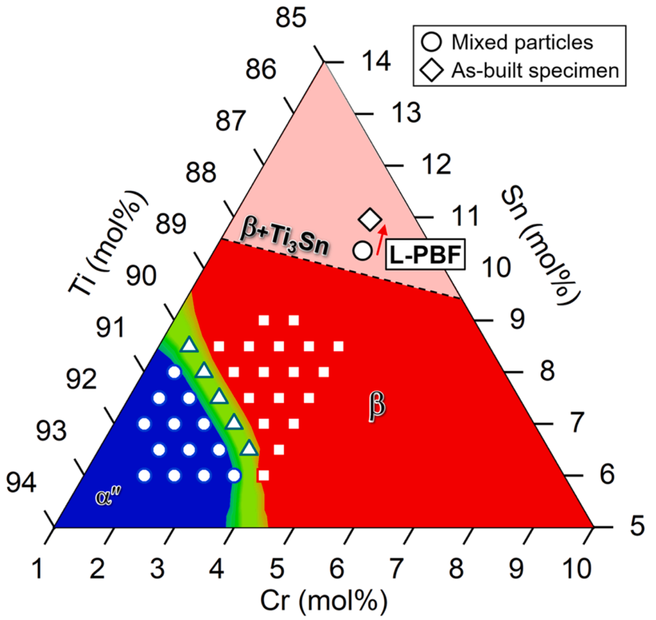

Fig. 3. Deviation from target composition by L-PBF. Phase map from the study of Sn-rich by conventional production method [3] and the β / β+Ti_3Sn boundary in the 1173 K phase diagram [10].

In metastable β-Ti alloys, also changes in the amount of additional elements lead to changes in martensitic transformation temperature. According to the literature, sensitivities are about −190 K/mol%Cr, −141 K/mol%Sn [3], and −160 K/mol%O [41]. Therefore, it is expected that the L-PBF in the present study changed the martensitic transformation temperature by −60 K from that designed in the powder mixing. The results of this study impart important information for the compositional formulation in the synthesis of Ti–Cr–Sn alloys using L-PBF for mixed pure metal powders.

Fig. 4 shows the results of XRD measurements. XY plane measurements revealed a strong 110_{β} peak in all samples, and other peaks from the β phase were also present, though weaker in intensity. The profiles of the 360 W and 300 W specimens with high laser power showed a single β phase. The specimens with lower power of 240 W and 180 W showed only a small peak of α phase was present, indicating that it was β+α dual phase. Notably, no Ti_3Sn nor $TiCr_2$ compounds were found in any of the samples. The XRD results indicate that, with appropriate building conditions, a supersaturated β single phase can be obtained at RT, which could not be obtained with the conventional method.

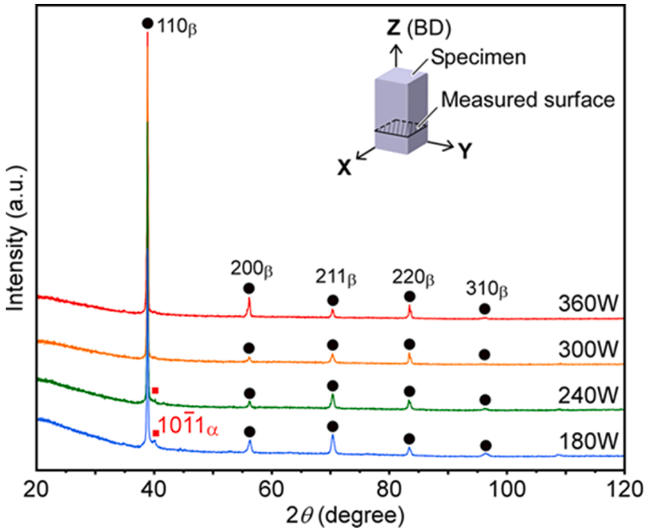

Fig. 4. XRD profiles of the as-built specimens at RT, together with a schematic diagram of the measured XY cross-section.

Fig. 5 shows the elemental mapping images of Ti, Cr, and Sn obtained by EDS measurements for (a) the 360 W and (b) the 180 W specimen. The leftmost figure shows the SEM images of the EDS measurement area. In Fig. 5(a), all elements were uniformly distributed and were expected to be solid solutions in β-Ti. On the other hand, in Fig. 5(b), the Cr was clearly separated into Cr-rich and Cr-lean regions. Sn was observed with slight separation, while Ti appeared almost homogeneous. Considering that the phase constitution was mostly β-Ti from the XRD measurements, there are no undissolved elements in the 180 W specimen, and the Cr-rich/Sn-lean β phase and Cr-lean/Sn-rich β phase were present as solid solutions. Additional low-magnification EDS maps covering multiple grains and grain boundaries are provided in Figure S2, which further confirm the overall compositional homogeneity at a larger scale. The present study demonstrated the possibility of in-situ alloying a metastable β-Ti type Ti–Cr–Sn alloy with more than 10 mol%Sn from pure elemental powder mixtures using AM.

Fig. 6 shows backscattered electron (BSE) images of as-built specimens. In the (a) 360 W and (b) 300 W specimens, elongated grains were observed together with linear features running along the x-direction (scan direction). These features included scan tracks, corresponding to the laser scanning path on the XY plane, as well as subgrain or grain boundaries formed near the melt pool centers, where cellular structures impinge during solidification. The morphology was typical microstructures of alloys produced by L-PBF [14,20,42]. In the (c) 240 W specimen, the grain size was smaller than (a) 360 W and (b) 300 W. In the (d) 180 W specimen, besides the grain refinement, the Cr-rich region and the lean regions were separated. This morphology is consistent with the EDS mapping (Fig. 5(b)).

SEM-BSE images revealed the morphology of the β phase. Subsequently, to investigate the distribution of these crystallographic orientations, EBSD measurements were performed on these microstructures. Fig. 7 shows the results of EBSD measurements of the as-built specimens. XY plane of each specimen was measured, and inverse pole figure (IPF) maps were created for each x-,y-, and z-direction. Regardless of the laser power *P*, the predominant trend observed was that 001_{β} was primarily oriented in the x-direction and 011_{β} in the y- and z-directions. This orientation pattern was most distinct at (a) 360 W, while at (d) 180 W, the grains were orientated more randomly.

Under building conditions where homogeneous metastable β phase was successfully obtained, the crystallographic texture developed was the same as those of the single-crystal-like microstructures reported for Ti–15Mo–5Zr–3Al (Ti-1553), a β-type Ti alloy, using the scan strategy (X-scan) [14,43,44].

The average grain sizes were calculated according to the linear intercept method from results of EBSD measurement (Fig. 7). The lines used were drawn horizontally and vertically, and their mean values were calculated. The grain boundaries were identified with a tolerance angle of 5°. The calculated grain sizes decreased with increasing laser power, measuring 62.6 μm, 35.4 μm, 26.9 μm, and 12.6 μm for specimens (a)–(d), respectively. These trends were consistent with SEM images (Fig. 6).

To investigate the orientation of each specimen in more detail, texture measurements were conducted on the XY plane by the XPFs method, and ODFs were calculated. The as-built Ti–Cr–Sn alloys were mainly composed of the β phase. Thus, ODFs were taken only for the β phase. The texture components were investigated on the $\varphi_2 = 45^{\circ}$ section of the ODF, as shown in Fig. 8. The results of the other sections are given in Figure S3(a)–(d) in the attached supplemental material. The texture component of $\{110\}_z\langle 001\rangle_x$ can be observed for (a) 360 W, (b) 300 W, and (c) 240 W. While for (d) 180 W, the orientation density of $\{110\}_z\langle 001\rangle_x$ was considerably lower. The texture components with the highest intensity for each specimen were shown with their value (I_{max}) at the bottom of Fig. 8. The I_{max} was highest at (a) 360 W,

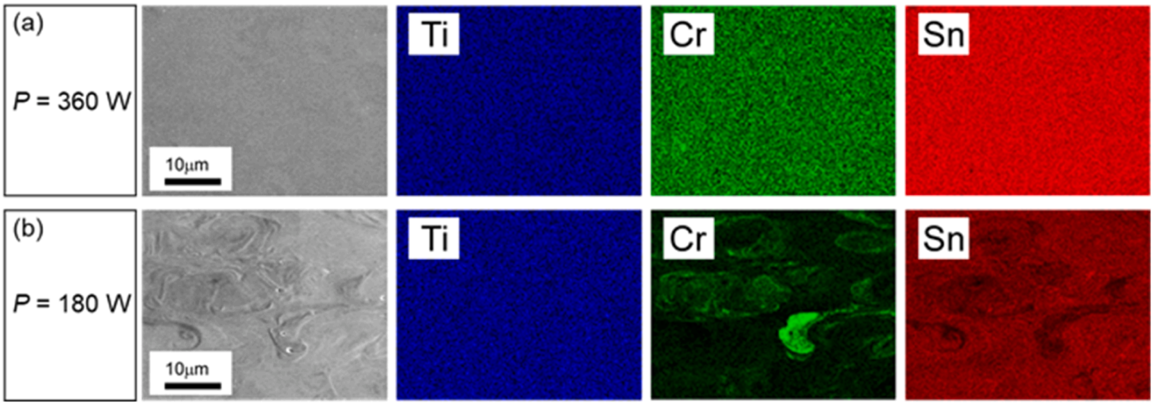

Fig. 5. Results of EDS measurement of (a) $P = 360$ W and (b) $P = 180$ W specimens.

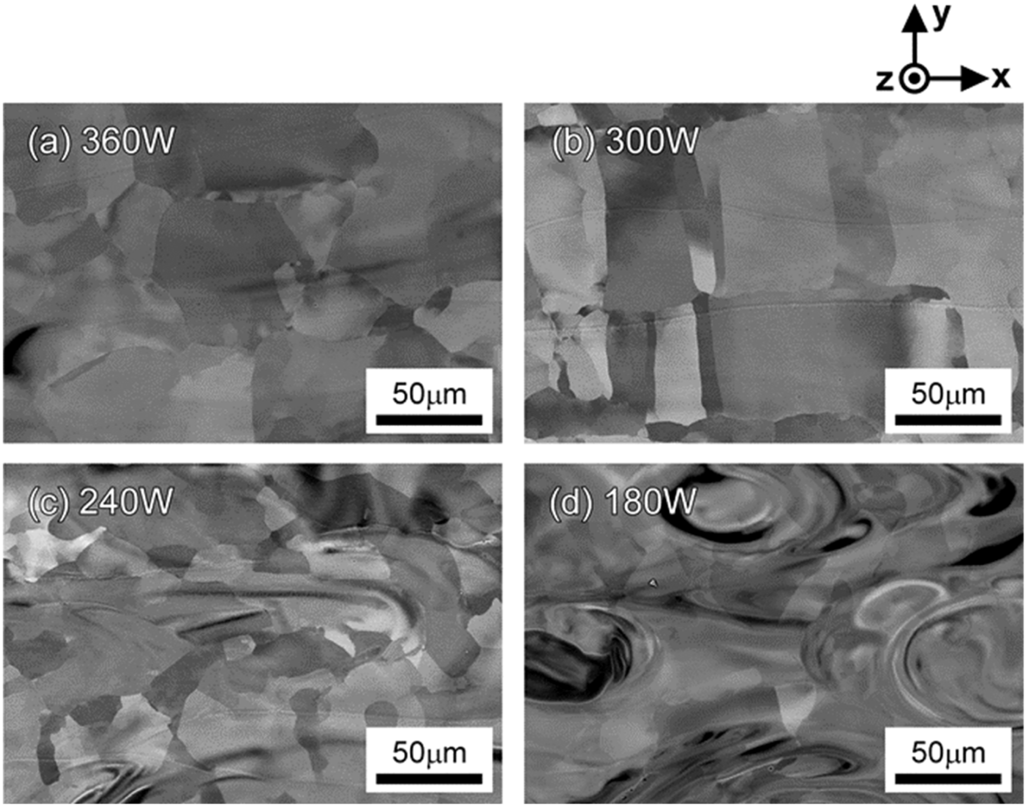

Fig. 6. SEM images of XY plane of the as-built specimens: (a) 360 W, (b) 300 W, (c) 240 W, (d) 180 W.

decreased as P decreased, and was lowest at (d) 180 W. The maximum intensity was observed at $\{17\ 12\ 3\}_z\langle 3\ 2\ \overline{25}\rangle_x$ in (a), $\{4\ 4\ 1\}_z\langle \overline{1}\ \overline{1}\ 8\rangle_x$ in (b) and (c). These are within about 10 ° of $\{110\}_z\langle 001\rangle_x$. On the other hand, the orientation with the highest intensity in (d) was $\{1\ 0\ 0\}_z\langle 0\ \overline{4}\ 11\rangle_x$, which showed a different orientation from (a)–(c). These results are consistent with the local texture that can be evaluated qualitatively from the IPF maps (Fig. 7).

From the above microstructure observation results, it was found that by appropriately controlling the building conditions, such as $P = 360$ W, a homogeneous, supersaturated metastable β-Ti solid solution can be fabricated from pure metal powder by the L-PBF method, even in alloy compositions that cannot be fabricated by conventional methods. It was also revealed that a strongly oriented microstructure can be obtained by the optimal scanning strategy, which has already been successfully applied to β-Ti alloys. In metastable β-Ti alloys, texture control is important for controlling their properties like martensitic transformation and Young's modulus. Since martensitic transformation involves a crystallographically defined lattice deformation, the transformation strain and variant selection are inherently orientation dependent [45]. Therefore, the development of specific crystallographic textures can significantly influence the transformation behavior [4]. Because L-PBF enables deliberate control of crystallographic texture through process parameter design, it is becoming an increasingly important fabrication process for metastable β-Ti alloys.

The internal microstructure of the 360 W specimen, confirmed to be a β single phase by XRD and SEM, was investigated by TEM. Fig. 9 shows the selected area diffraction patterns (SADPs) obtained from several beam directions. In all patterns, spots mainly originating from the β phase were observed. When the ω phase is present in metastable β-Ti alloys, ω-spots appear at the 1/3 and 2/3 $\langle 121\rangle^*_\beta$ positions in SADP from $\mathbf{B} = [101]_\beta$. In the present study, the spots were very weak, and

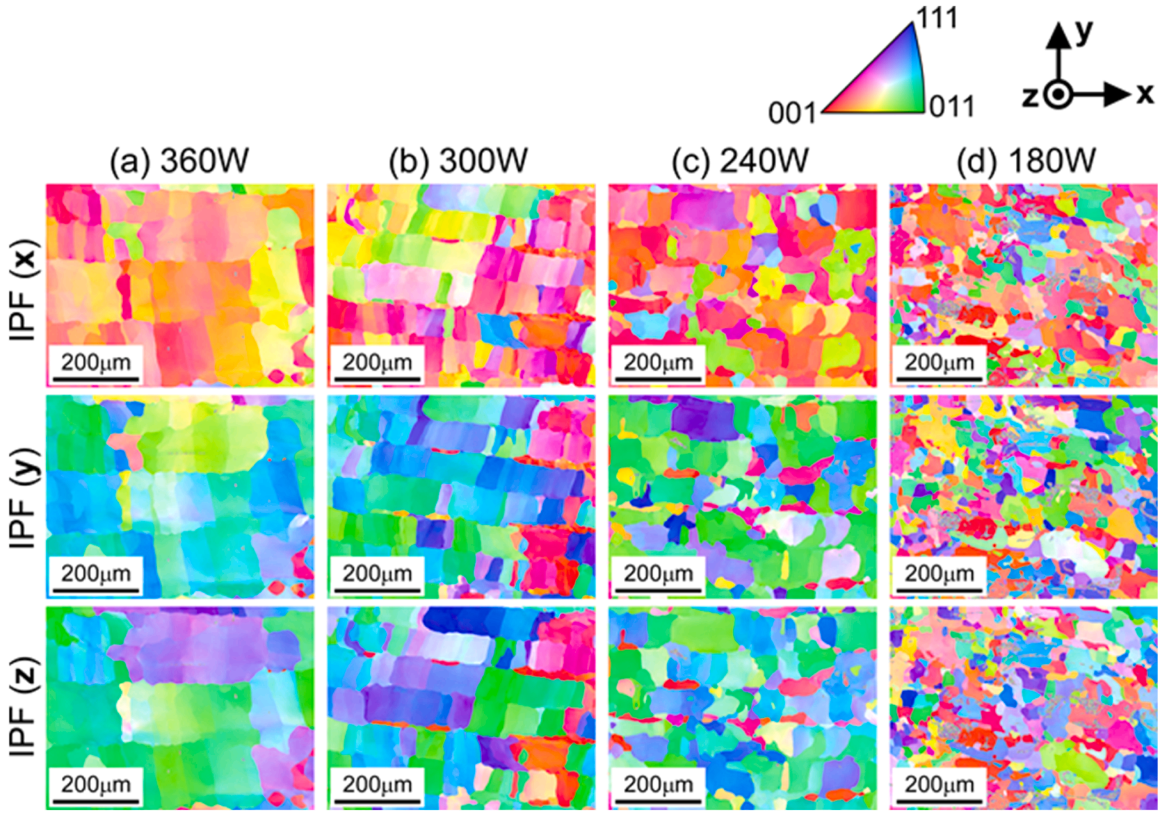

Fig. 7. IPF maps of the as-built specimens measured on the XY plane. (a) 360 W, (b) 300 W, (c) 240 W, and (d) 180 W.

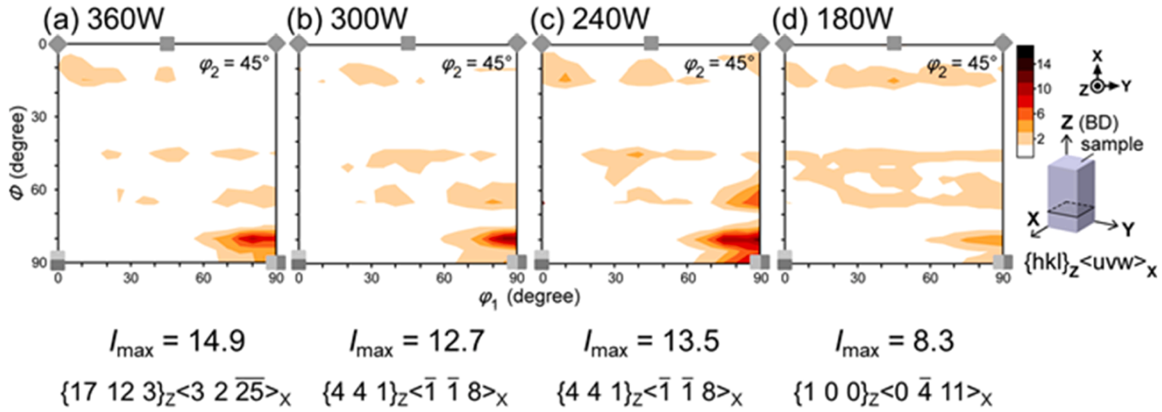

Fig. 8. $\varphi_2 = 45\circ$ sections of ODFs for the as-built specimens, showing the highest intensity texture component $\{hkl\}_z\langle uvw\rangle_x$ and its maximum intensity (I_{max}). (a) 360 W, (b) 300 W, (c) 240 W, and (d) 180 W.

only slight streaks were observed. This is consistent with the references that athermal ω was sufficiently suppressed in Sn-rich Ti–Cr–Sn alloys [4].

In addition, a weak spot can be seen at $1/2\ \langle 121\rangle^*_\beta$. A dark-field (DF) image using this spot is shown in Fig. 10. The observed direction was slightly tilted from $[101]_\beta$ to enhance the contrast of the image. The SADP used for imaging is shown together in the inset. The DF image shows dispersed products a few nanometers in size. Similar products in the solution-treated β phase have been reported in several metastable β-Ti alloys added with O and N [46,47], interstitial elements or with large amounts of Sn and Al, substitutional elements [48,49], and it is attributed to the martensite type lattice modulation [50]. The oxygen concentration of the as-built alloy was 0.34 mol%, which was 1.5–2 times higher than that of the Ti alloy prepared by the conventional method. Therefore, further studies are needed to clarify the factors that cause martensitic lattice modulation in Ti–Cr–Sn AM materials.

The mechanical properties of the as-built specimens were investigated. Cyclic loading–unloading compression tests were performed with the applied strain increased by an increment of 1% per cycle up to 9%, and after the 10th cycle, the strain was applied continuously until fracture. The obtained stress–strain curves are shown in Fig. 11. None of the alloys exhibited pseudoelastic shape recovery during unloading. In addition, pronounced strain hardening and two-stage yielding behavior reported in some metastable β-Ti alloys [51,52] were not observed in the present study. Since pronounced strain hardening is typically associated with twinning-induced plasticity (TWIP) or transformation-induced plasticity (TRIP) mechanisms, whereas two-stage yielding is associated with stress-induced martensitic transformation, the absence of these

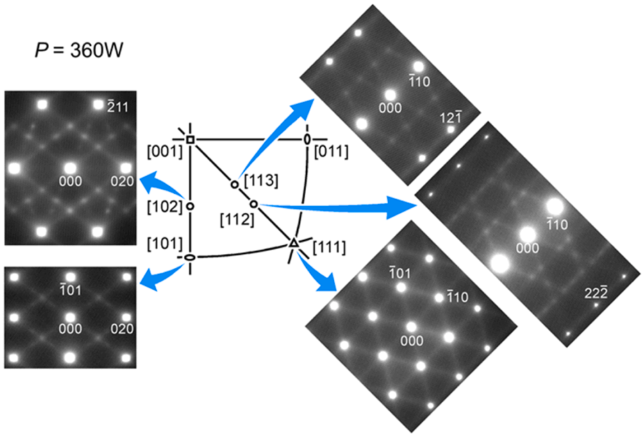

Fig. 9. SADPs for $P = 360$ W specimen obtained from beam direction of **B**= $[102]_\beta$, $[101]_\beta$, $[113]_\beta$, $[112]_\beta$, and $[111]_\beta$.

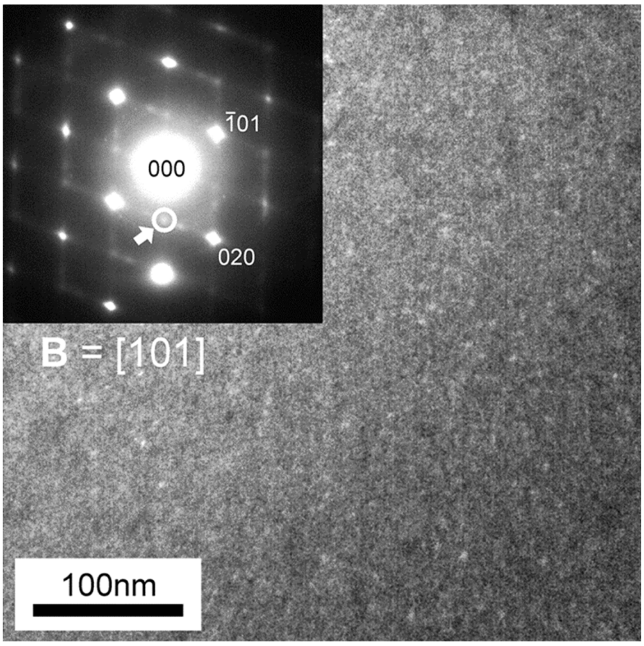

Fig. 10. TEM DF image of the nanosized lattice modulations of $P = 360$ W specimen, taken from the spot indicated by the circle in the inset SADP obtained from $\sim[101]_\beta$ direction.

features indicates that the present Ti–Cr–Sn AM material underwent plastic deformation, most plausibly dominated by dislocation slip under the applied testing conditions. The outer envelope of the cyclic stress–strain curve is known to coincide with a continuous stress–strain curve [53,54]. Compressive strength (σ_{CS}) and fracture strain (ε_F) were read from the contour of the stress–strain curves. The σ_{CS} was 890 MPa at (a) 360 W, 873 MPa at (b) 300 W, 950 MPa at (c) 240 W, and 988 MPa at (d) 180 W. The higher strength at lower P can be attributed to the decrease in grain size.

Regarding ductility, only (d) 180 W was fractured during the cyclic deformation (i.e., before reaching the 10th cycle), with an ε_F of 5.0%. In Ti–Cr alloy, it is known that the addition of more than 12 mass%Cr (11.15 mol%Cr) results in a significant decrease in ductility [55]. In the 180 W specimen, compositional variations such as Cr-rich regions existed throughout the material. Compositional analysis of the Cr-rich region shown in the EDS map in Fig. 5(b) indicated that the composition is Ti–16.2Cr–8.1Sn (mol%). Considering that no significant porosity was observed and that all specimens were tested under identical geometry and loading conditions, the reduction in ductility is most reasonably attributed to microstructural inhomogeneity in this material.

To evaluate the plastic deformation behavior and to distinguish it from elastic deformation, the maximum applied stress and residual strain after unloading for each cycle are plotted in Fig. 12(a). This plot corresponds to a stress–plastic strain curve. The discrete plots obtained were fitted, and the yield stress ($\sigma_{0.2}$), defined as 0.2% flow stress, was evaluated. The derived values are plotted against laser power in Fig. 12(b). The $\sigma_{0.2}$ was highest for the specimen with the lowest laser power, (d) 180 W. This may be due to the influence of precipitates and grain size, as in the discussion of σ_{CS}.

Additionally, the grain sizes obtained from Fig. 7 are plotted in Fig. 12(b) to examine the relationship between $\sigma_{0.2}$ and grain size; interestingly, only (a) 360 W deviates from the trend. Although the 360 W specimen was the most homogeneous, exhibited the strongest texture, and had the largest grain size, which would typically suggest lower strength, it showed a moderate $\sigma_{0.2}$ of 725 MPa.

While the specifics of deformation modes in AM materials warrant further investigation, these findings indicate that appropriate processing conditions can achieve a balanced combination of chemical homogeneity, microstructural control, and mechanical properties in metastable β-Ti alloys, even in the as-built state.

While the above discussion focused on plastic deformation, the elastic response provides important insights not only into the deformation behavior but also into the phase stability and crystallographic anisotropy of the β phase. Since the Young's modulus estimated from the macroscopic stress–strain curves may include machine and fixture compliance, a more accurate evaluation was performed using direct optical strain measurement. In this method, strain was measured from the specimen surface during compression testing, thereby eliminating compliance effects. The updated experimental Young's modulus values are plotted in Fig. 13. To quantitatively evaluate the experimentally obtained Young's modulus in terms of the crystallographic texture, the polycrystalline elastic modulus was calculated by combining the single-crystal elastic constants derived from ab-initio simulations with the measured ODFs.

The single-crystal elastic constants of the β-Ti–Cr–Sn alloy obtained from the first-principles calculations were $C_{11} = 121$ GPa, $C_{12} = 108$ GPa, and $C_{44} = 48$ GPa, satisfying the dynamic stability criterion for cubic crystals ($C_{11}+2C_{12} > 0$, $C_{11}-C_{12} > 0$, $C_{44} > 0$) [56]. These constants were used as input parameters for the orientation-weighted polycrystalline averaging based on the measured ODFs.

For each orientation $\boldsymbol{g}$ in the ODF, the stiffness tensor $C_{ijkl}(\boldsymbol{g})$ was obtained by rotating the single-crystal elastic constants using the corresponding rotation matrix. The macroscopic stiffness and compliance tensors were then averaged over all orientations by the Voigt and Reuss models, respectively, as

$$C_{ijkl}^{V} = \langle C_{ijkl}(\boldsymbol{g}) \rangle,\ S_{ijkl}^{R} = \langle S_{ijkl}(\boldsymbol{g}) \rangle, \tag{3}$$

where ⟨ ⟩ denotes orientation averaging weighted by the ODF. The Hill average C_{ijkl}^{H} was finally obtained as the arithmetic mean of the Voigt and Reuss tensors. The detailed formulation of the ODF-weighted averaging procedure is provided in the supplemental material.

Using these averaged tensors, the orientation-weighted Young's moduli [57,58] along the compression direction (x) were evaluated based on the Voigt, Reuss, and Hill models [59]. The results are shown in Fig. 13. The calculated values range from 40 to 65 GPa depending on the averaging scheme. Reflecting the texture development, particularly the strengthening of the $<001>_\beta$ orientation that exhibits the lowest elastic modulus [60], the specimens fabricated at higher laser power exhibited slightly lower averaged Young's moduli, although the overall dependence on laser power was limited.

For the higher laser power conditions ($P = 300$ and 360 W), which exhibited chemically homogeneous single β-phase microstructures, the experimentally measured Young's moduli fall within the Voigt–Reuss

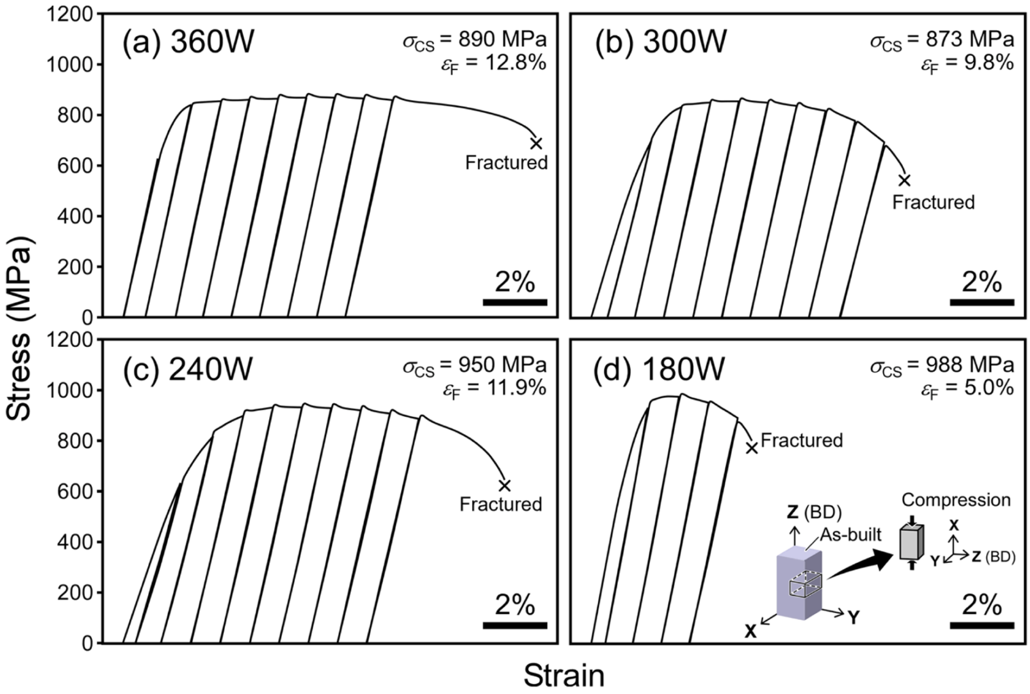

Fig. 11. Compressive stress–strain curves obtained at RT for the as-built specimens. (a) 360 W, (b) 300 W, (c) 240 W, and (d) 180 W.

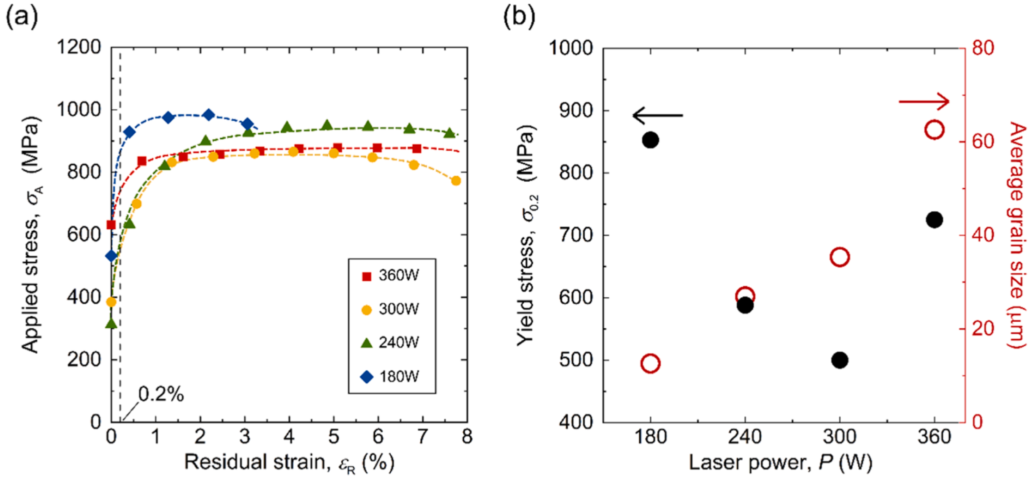

Fig. 12. (a) Relationship between maximum applied stress per cycle and residual strain as derived from Fig. 11; (b) Correlation of yield stress and average grain size with laser power.

bounds and are close to the Reuss (uniform stress) estimate. This agreement indicates that the elastic response of these specimens is well described by the texture-weighted polycrystalline model based on the single-crystal elastic constants.

In contrast, the lower laser power ($P = 180$ and 240 W) showed experimentally measured modulus values that slightly exceeded the Voigt upper bound predicted for an ideal β single-phase polycrystal. This deviation is reasonably attributed to the microstructural inhomogeneities observed in these samples, including minor α phase presence and compositional fluctuations, which are not incorporated in the single-phase texture-based elastic model.

Importantly, the optimized specimen fabricated at $P = 360$ W exhibited a Young's modulus of approximately 40 GPa, which is close to the Reuss prediction and significantly lower than typical α+ β titanium alloys. The good agreement between experiment and model in this condition demonstrates that when a homogeneous β solid solution is achieved, the elastic response can be quantitatively predicted from crystallographic texture and single-crystal elastic constants. This predictive capability highlights the effectiveness of L-PBF in designing low-modulus metastable β-Ti alloys through texture and phase stability control.

In this study, we found that homogeneous supersaturated metastable β-Ti solid solutions can be fabricated directly from pure metal powders by the L-PBF method, even for alloy compositions with ultra-high Sn content that cannot be prepared by conventional fabrication methods. Through optimization of the processing parameters, optimal microstructures with desirable mechanical properties were achieved in the as-built condition, without requiring any rescanning or post-heat treatment. Furthermore, Ti–Cr–Sn alloys are known to be more cost-effective than many other β-Ti systems [61], and the demonstrated use of readily available pure metal powders instead of pre-alloyed powders further reduces material costs, enhancing their potential for applications.

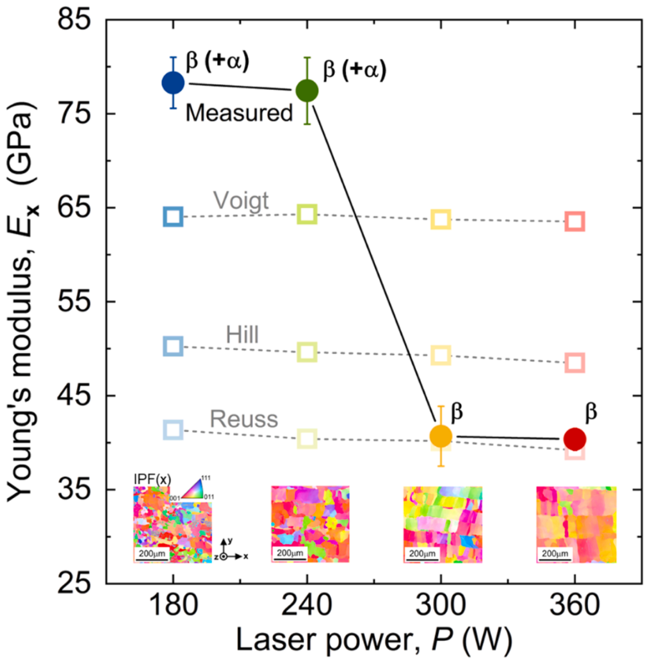

Fig. 13. Calculated polycrystalline Young's moduli based on ab-initio single-crystal constants and measured textures (Voigt–Reuss–Hill models), together with experimental data and corresponding IPF maps showing the $< 001 >_\beta$ texture development.

Although the present alloy did not exhibit shape memory or superelastic behavior under the current compositional conditions, the ability of L-PBF to access Sn-rich metastable β compositions beyond the conventional equilibrium boundary provides a promising platform for functional alloy design. By carefully tuning β phase stability through adjustment of Sn and Cr contents, it should be possible to position the alloy within the appropriate metastability window required for shape memory or superelastic behavior. Further investigation in this direction will be pursued in future work.

4. Conclusions

This study has successfully demonstrated that laser powder bed fusion (L-PBF) using mixed pure elemental powders can effectively maintain the homogeneity and stability of the β phase in the metastable β-type Ti–Cr–Sn alloys with high Sn content, which is difficult to achieve with conventional alloy fabrication methods. The detailed findings are summarized as follows.

1. A stable and homogeneous β solid solution was produced using L-PBF from spherical pure metal powders.
2. The composition before fabrication was Ti–3.45Cr–10.33Sn–0.28 O (mol%), and after AM it was Ti–3.29Cr–10.89Sn–0.34 O (mol%).
3. Undesirable ω phase and Ti_3Sn compounds were successfully suppressed.
4. Control over microstructural orientation was achieved, with the texture component of $\{110\}_z\langle001\rangle_x$ by X-scan strategy.
5. The mechanical properties of the alloys were optimized for the specimens in the building condition where a homogeneous microstructure was obtained.

Author Statement

We, the undersigned authors, confirm that: All authors have reviewed and approved the final version of the manuscript to be submitted to *Additive Manufacturing*. The manuscript represents original work and has not been published previously, nor is it under consideration for publication elsewhere.

CRediT authorship contribution statement

Takuya Ishimoto: Validation, Methodology, Investigation, Formal analysis, Conceptualization. **Yuichiro Koizumi:** Writing – review & editing, Validation, Supervision, Resources, Project administration, Funding acquisition. **Masaki Tahara:** Writing – review & editing, Visualization, Validation, Supervision, Resources, Project administration, Methodology, Funding acquisition, Formal analysis, Data curation, Conceptualization. **Ryosuke Ozasa:** Validation, Methodology, Investigation, Formal analysis. **Akira Umise:** Validation, Formal analysis. **Takeshi Teramoto:** Writing – review & editing, Software, Methodology, Investigation, Formal analysis, Data curation, Conceptualization. **Yilin Jin:** Investigation, Formal analysis. **Wan-Ting Chiu:** Investigation, Formal analysis. **Hideki Hosoda:** Writing – review & editing, Validation, Supervision, Resources, Project administration, Conceptualization. **Naoki Nohira:** Writing – original draft, Visualization, Software, Methodology, Investigation, Formal analysis, Data curation. **Cheng Chen:** Investigation, Formal analysis. **Takayoshi Nakano:** Writing – review & editing, Validation, Supervision, Resources, Project administration, Funding acquisition, Conceptualization.

Declaration of Competing Interest

The authors declare that they have no known competing financial interests or personal relationships that could have appeared to influence the work reported in this paper

Acknowledgments

The authors would like to thank the Materials Analysis Division and the Design and Manufacturing Division of the Core Facility Center, Institute of Science Tokyo, for their support in TEM sample preparation using FIB and in preparing the testing jig.

This work was supported by the Iketani Science and Technology Foundation, Japan Society for the Promotion of Science (JSPS) KAKENHI (JP24K17493, JP22H00256, JP22K18899, JP22H05276, JP24H00986), and JST CREST (JPMJCR2194).

Appendix A. Supporting information

Supplementary data associated with this article can be found in the online version at doi:10.1016/j.addma.2026.105213.

Data availability

The data that has been used is confidential.

References

[1] A. Biesiekierski, J. Wang, M. Abdel-Hady Gepreel, C. Wen, A new look at biomedical Ti-based shape memory alloys, Acta Biomater. 8 (2012) 1661–1669, https://doi.org/10.1016/j.actbio.2012.01.018.

[2] S.S. Sidhu, H. Singh, M.A.-H. Gepreel, A review on alloy design, biological response, and strengthening of β-titanium alloys as biomaterials, Mater. Sci. Eng. C 121 (2021) 111661, https://doi.org/10.1016/j.msec.2020.111661.

[3] M.S. Park, W.-T. Chiu, N. Nohira, M. Tahara, H. Hosoda, Effects of Cr and Sn additives on the martensitic transformation and deformation behavior of Ti-Cr-Sn biomedical shape memory alloys, Mater. Sci. Eng. A 822 (2021) 141668, https://doi.org/10.1016/j.msea.2021.141668.

[4] M.S. Park, W.-T. Chiu, N. Nohira, M. Iwasaki, M. Tahara, H. Hosoda, Microstructure characteristics and superelastic properties of novel Ti–Cr–Sn superelastic alloys, Mater. Sci. Eng. A 869 (2023) 144790, https://doi.org/10.1016/j.msea.2023.144790.

[5] C. Brozek, F. Sun, P. Vermaut, Y. Millet, A. Lenain, D. Embury, P.J. Jacques, F. Prima, A β-titanium alloy with extra high strain-hardening rate: Design and mechanical properties, Scr. Mater. 114 (2016) 60–64, https://doi.org/10.1016/j.scriptamat.2015.11.020.

[6] M. Ikeda, S. Masuda, M. Ogawa, The Effect of Tin Addition on the Phase Constitution and Heat Treatment Behavior in Ti-7mass%Cr Alloy for Biomedical and Healthcare Applications, in: M. Niinomi, S. Akiyama, M. Ikeda, M. Hagiwara, K. Maruyama (Eds.), Proceedings of the 11th World Conference on Titanium, The Japan Institute of Metals, Kyoto, 2007, pp. 1433–1436.

[7] J.L. Murray, The Cr−Ti (chromium-titanium) system, Bull. Alloy Phase Diagr. 2 (1981) 174–181, https://doi.org/10.1007/BF02881474.

[8] H. Okamoto, Sn-Ti (Tin-Titanium), J. Phase Equilibria Diffus 31 (2010) 202–203, https://doi.org/10.1007/s11669-010-9663-2.

[9] S.F. Aricó, L.M. Gribaudo, Isothermal sections at 900 and 1100°C of the Cr–Sn–Ti system, J. Alloy. Compd. 461 (2008) 92–96, https://doi.org/10.1016/j.jallcom.2007.06.117.

[10] Y. Gao, C. Guo, C. Li, Z. Du, Thermodynamic description of the Cr–Sn–Ti system, J. Alloy. Compd. 498 (2010) 130–138, https://doi.org/10.1016/j.jallcom.2010.03.140.

[11] X.X. Ye, B. Chen, J.H. Shen, J. Umeda, K. Kondoh, Microstructure and strengthening mechanism of ultrastrong and ductile Ti-xSn alloy processed by powder metallurgy, J. Alloy. Compd. 709 (2017) 381–393, https://doi.org/10.1016/j.jallcom.2017.03.171.

[12] D. Herzog, V. Seyda, E. Wycisk, C. Emmelmann, Additive manufacturing of metals, Acta Mater. 117 (2016) 371–392, https://doi.org/10.1016/j.actamat.2016.07.019.

[13] J.C. Colombo-Pulgarín, C.A. Biffi, M. Vedani, D. Celentano, A. Sánchez-Egea, A. D. Boccardo, J.P. Ponthot, Beta Titanium Alloys Processed By Laser Powder Bed Fusion: A Review, J. Mater. Eng. Perform. 30 (2021) 6365–6388, https://doi.org/10.1007/s11665-021-05800-6.

[14] T. Ishimoto, K. Hagihara, K. Hisamoto, S.-H. Sun, T. Nakano, Crystallographic texture control of beta-type Ti–15Mo–5Zr–3Al alloy by selective laser melting for the development of novel implants with a biocompatible low Young's modulus, Scr. Mater. 132 (2017) 34–38, https://doi.org/10.1016/j.scriptamat.2016.12.038.

[15] T. Ishimoto, N. Morita, R. Ozasa, A. Matsugaki, O. Gokcekaya, S. Higashino, M. Tane, T. Mayama, K. Cho, H.Y. Yasuda, M. Okugawa, Y. Koizumi, M. Yoshiya, D. Egusa, T. Sasaki, E. Abe, H. Kimizuka, N. Ikeo, T. Nakano, Superimpositional design of crystallographic textures and macroscopic shapes via metal additive manufacturing—Game-change in component design, Acta Mater. 286 (2025) 120709, https://doi.org/10.1016/j.actamat.2025.120709.

[16] D. Gu, Y.-C. Hagedorn, W. Meiners, G. Meng, R.J.S. Batista, K. Wissenbach, R. Poprawe, Densification behavior, microstructure evolution, and wear performance of selective laser melting processed commercially pure titanium, Acta Mater. 60 (2012) 3849–3860, https://doi.org/10.1016/j.actamat.2012.04.006.

[17] F. Yin, J.-C. Tedenac, F. Gascoin, Thermodynamic modelling of the Ti–Sn system and calculation of the Co–Ti–Sn system, Calphad 31 (2007) 370–379, https://doi.org/10.1016/j.calphad.2007.01.003.

[18] M. Fischer, D. Joguet, G. Robin, L. Peltier, P. Laheurte, In situ elaboration of a binary Ti–26Nb alloy by selective laser melting of elemental titanium and niobium mixed powders, Mater. Sci. Eng. C 62 (2016) 852–859, https://doi.org/10.1016/j.msec.2016.02.033.

[19] M. Simonelli, N.T. Aboulkhair, P. Cohen, J.W. Murray, A.T. Clare, C. Tuck, R.J. M. Hague, A comparison of Ti-6Al-4V in-situ alloying in Selective Laser Melting using simply-mixed and satellited powder blend feedstocks, Mater. Charact. 143 (2018) 118–126, https://doi.org/10.1016/j.matchar.2018.05.039.

[20] J.C. Wang, Y.J. Liu, S.X. Liang, Y.S. Zhang, L.Q. Wang, T.B. Sercombe, L.C. Zhang, Comparison of microstructure and mechanical behavior of Ti-35Nb manufactured by laser powder bed fusion from elemental powder mixture and prealloyed powder, J. Mater. Sci. Technol. 105 (2022) 1–16, https://doi.org/10.1016/j.jmst.2021.07.021.

[21] I. Yadroitsev, P. Krakhmalev, I. Yadroitsava, Titanium Alloys Manufactured by In Situ Alloying During Laser Powder Bed Fusion, JOM 69 (2017) 2725–2730, https://doi.org/10.1007/s11837-017-2600-7.

[22] T. Nagase, T. Hori, M. Todai, S.-H. Sun, T. Nakano, Additive manufacturing of dense components in beta-titanium alloys with crystallographic texture from a mixture of pure metallic element powders, Mater. Des. 173 (2019) 107771, https://doi.org/10.1016/j.matdes.2019.107771.

[23] D. Gu, Y. Shen, Effects of processing parameters on consolidation and microstructure of W–Cu components by DMLS, J. Alloy. Compd. 473 (2009) 107–115, https://doi.org/10.1016/j.jallcom.2008.05.065.

[24] L. Thijs, F. Verhaeghe, T. Craeghs, J.Van Humbeeck, J.-P. Kruth, A study of the microstructural evolution during selective laser melting of Ti–6Al–4V, Acta Mater. 58 (2010) 3303–3312, https://doi.org/10.1016/j.actamat.2010.02.004.

[25] L.G. Schulz, A Direct Method of Determining Preferred Orientation of a Flat Reflection Sample Using a Geiger Counter X-Ray Spectrometer, J. Appl. Phys. 20 (1949) 1030–1033, https://doi.org/10.1063/1.1698268.

[26] S. Matthies, G.W. Vinel, On the Reproduction of the Orientation Distribution Function of Texturized Samples from Reduced Pole Figures Using the Conception of a Conditional Ghost Correction, Phys. Status Solidi (b) 112 (1982) K111–K114, https://doi.org/10.1002/pssb.2221120254.

[27] G. Kresse, J. Hafner, Ab initio molecular dynamics for liquid metals, Phys. Rev. B 47 (1993) 558–561, https://doi.org/10.1103/PhysRevB.47.558.

[28] G. Kresse, J. Hafner, Ab initio molecular-dynamics simulation of the liquid-metal–amorphous-semiconductor transition in germanium, Phys. Rev. B 49 (1994) 14251–14269, https://doi.org/10.1103/PhysRevB.49.14251.

[29] G. Kresse, J. Furthmüller, Efficient iterative schemes for ab initio total-energy calculations using a plane-wave basis set, Phys. Rev. B 54 (1996) 11169–11186, https://doi.org/10.1103/PhysRevB.54.11169.

[30] G. Kresse, J. Furthmüller, Efficiency of ab-initio total energy calculations for metals and semiconductors using a plane-wave basis set, Comput. Mater. Sci. 6 (1996) 15–50, https://doi.org/10.1016/0927-0256(96)00008-0.

[31] P.E. Blöchl, Projector augmented-wave method, Phys. Rev. B 50 (1994) 17953–17979, https://doi.org/10.1103/PhysRevB.50.17953.

[32] G. Kresse, D. Joubert, From ultrasoft pseudopotentials to the projector augmented-wave method, Phys. Rev. B 59 (1999) 1758–1775, https://doi.org/10.1103/PhysRevB.59.1758.

[33] J.P. Perdew, K. Burke, M. Ernzerhof, Generalized Gradient Approximation Made Simple, Phys. Rev. Lett. 77 (1996) 3865–3868, https://doi.org/10.1103/PhysRevLett.77.3865.

[34] A. Zunger, S.-H. Wei, L.G. Ferreira, J.E. Bernard, Special quasirandom structures, Phys. Rev. Lett. 65 (1990) 353–356, https://doi.org/10.1103/PhysRevLett.65.353.

[35] A. van de Walle, Multicomponent multisublattice alloys, nonconfigurational entropy and other additions to the Alloy Theoretic Automated Toolkit, Calphad 33 (2009) 266–278, https://doi.org/10.1016/j.calphad.2008.12.005.

[36] D. Raabe, B. Sander, M. Friák, D. Ma, J. Neugebauer, Theory-guided bottom-up design of β-titanium alloys as biomaterials based on first principles calculations: Theory and experiments, Acta Mater. 55 (2007) 4475–4487, https://doi.org/10.1016/j.actamat.2007.04.024.

[37] J. Liu, P. Wen, Metal vaporization and its influence during laser powder bed fusion process, Mater. Des. 215 (2022) 110505, https://doi.org/10.1016/j.matdes.2022.110505.

[38] H. Mizukami, Y. Shirai, A. Mitchell, Evaporation Behavior of Aluminum from Titanium Alloy Melt with Different Initial Aluminum Contents, Tetsu-to-Hagane 108 (2022) 383–393, https://doi.org/10.2355/tetsutohagane.TETSU-2022-004.

[39] M. Elahinia, N. Shayesteh Moghaddam, M. Taheri Andani, A. Amerinatanzi, B. A. Bimber, R.F. Hamilton, Fabrication of NiTi through additive manufacturing: A review, Prog. Mater. Sci. 83 (2016) 630–663, https://doi.org/10.1016/j.pmatsci.2016.08.001.

[40] C. Haberland, M. Elahinia, J.M. Walker, H. Meier, J. Frenzel, On the development of high quality NiTi shape memory and pseudoelastic parts by additive manufacturing, Smart Mater. Struct. 23 (2014) 104002, https://doi.org/10.1088/0964-1726/23/10/104002.

[41] J.Il Kim, H.Y. Kim, H. Hosoda, S. Miyazaki, Shape Memory Behavior of Ti-22Nb-(0.5-2.0)O(at%) Biomedical Alloys, Mater. Trans. 46 (2005) 852–857, https://doi.org/10.2320/matertrans.46.852.

[42] J. Wang, Y. Liu, C.D. Rabadia, S.-X. Liang, T.B. Sercombe, L.-C. Zhang, Microstructural homogeneity and mechanical behavior of a selective laser melted Ti-35Nb alloy produced from an elemental powder mixture, J. Mater. Sci. Technol. 61 (2021) 221–233, https://doi.org/10.1016/j.jmst.2020.05.052.

[43] T. Ishimoto, K. Hagihara, K. Hisamoto, T. Nakano, Stability of crystallographic texture in laser powder bed fusion: Understanding the competition of crystal growth using a single crystalline seed, Addit. Manuf. 43 (2021) 102004, https://doi.org/10.1016/j.addma.2021.102004.

[44] S.-H. Sun, K. Hagihara, T. Ishimoto, R. Suganuma, Y.-F. Xue, T. Nakano, Comparison of microstructure, crystallographic texture, and mechanical properties in Ti–15Mo–5Zr–3Al alloys fabricated via electron and laser beam powder bed fusion technologies, Addit. Manuf. 47 (2021) 102329, https://doi.org/10.1016/j.addma.2021.102329.

[45] Y. Fukui, T. Inamura, H. Hosoda, K. Wakashima, S. Miyazaki, Mechanical Properties of a Ti-Nb-Al Shape Memory Alloy, Mater. Trans. 45 (2004) 1077–1082, https://doi.org/10.2320/matertrans.45.1077.

[46] J. Fu, H.Y. Kim, S. Miyazaki, Effect of N addition on nano-domain structure and mechanical properties of a meta-stable Ti-Zr based alloy, Scr. Mater. 203 (2021) 114068, https://doi.org/10.1016/j.scriptamat.2021.114068.

[47] Y. Zheng, T. Alam, R. Banerjee, D. Banerjee, H.L. Fraser, The influence of aluminum and oxygen additions on intrinsic structural instabilities in titanium-molybdenum alloys, Scr. Mater. 152 (2018) 150–153, https://doi.org/10.1016/j.scriptamat.2018.04.030.

[48] N. Nohira, Y. Oshita, W.-T. Chiu, A. Umise, M. Tahara, H. Hosoda, Effect of aging on isothermal ω/α″ growth and resulting mechanical behaviors of the Ti–Mo–Al high temperature shape memory alloys, Mater. Charact. 199 (2023) 112850, https://doi.org/10.1016/j.matchar.2023.112850.

[49] P. Wang, M. Todai, T. Nakano, ω-phase transformation and lattice modulation in biomedical β-phase Ti-Nb-Al alloys, J. Alloy. Compd. 766 (2018) 511–516, https://doi.org/10.1016/j.jallcom.2018.06.266.

[50] M. Tahara, H.Y. Kim, T. Inamura, H. Hosoda, S. Miyazaki, Lattice modulation and superelasticity in oxygen-added β-Ti alloys, Acta Mater. 59 (2011) 6208–6218, https://doi.org/10.1016/j.actamat.2011.06.015.

[51] F. Sun, J.Y. Zhang, M. Marteleur, T. Gloriant, P. Vermaut, D. Laillé, P. Castany, C. Curfs, P.J. Jacques, F. Prima, Investigation of early stage deformation mechanisms in a metastable β titanium alloy showing combined twinning-induced plasticity and transformation-induced plasticity effects, Acta Mater. 61 (2013) 6406–6417, https://doi.org/10.1016/j.actamat.2013.07.019.

[52] J.Y. Zhang, J.S. Li, Z. Chen, Q.K. Meng, F. Sun, B.L. Shen, Microstructural evolution of a ductile metastable β titanium alloy with combined TRIP/TWIP effects, J. Alloy. Compd. 699 (2017) 775–782, https://doi.org/10.1016/j.jallcom.2016.12.394.

[53] S. Li, M. Choi, T. Nam, Role of fine nano-scaled isothermal omega phase on the mechanical and superelastic properties of a high Zr-containing Ti-Zr-Nb-Sn shape memory alloy, Mater. Sci. Eng. A 782 (2020) 139278, https://doi.org/10.1016/j.msea.2020.139278.

[54] Y. Yang, P. Castany, M. Cornen, F. Prima, S.J. Li, Y.L. Hao, T. Gloriant, Characterization of the martensitic transformation in the superelastic Ti–24Nb–4Zr–8Sn alloy by in situ synchrotron X-ray diffraction and dynamic mechanical analysis, Acta Mater. 88 (2015) 25–33, https://doi.org/10.1016/j.actamat.2015.01.039.

[55] S. Hanada, O. Izumi, Deformation behaviour of retained β phase in β-eutectoid Ti-Cr alloys, J. Mater. Sci. 21 (1986) 4131–4139, https://doi.org/10.1007/BF01106518.

[56] M. Born, On the stability of crystal lattices. I, Math. Proc. Camb. Philos. Soc. 36 (1940) 160–172, https://doi.org/10.1017/S0305004100017138.

[57] J.L. Buroni, F.C. Buroni, Averaging material tensors of any rank in textured polycrystalline materials: Extending the scope beyond crystallographic proper point groups, Int. J. Eng. Sci. 193 (2023) 103942, https://doi.org/10.1016/j.ijengsci.2023.103942.

[58] P.R. Cantwell, H. Kim, M.M. Schneider, H.H. Hsu, D. Peroulis, E.A. Stach, A. Strachan, Estimating the in-plane young's modulus of polycrystalline films in mems, J. Micro Syst. 21 (2012) 840–849, https://doi.org/10.1109/JMEMS.2012.2191939.

[59] R. Hill, The Elastic Behaviour of a Crystalline Aggregate, Proc. Phys. Soc. Sect. A 65 (1952) 349–354, https://doi.org/10.1088/0370-1298/65/5/307.

[60] M. Tane, S. Akita, T. Nakano, K. Hagihara, Y. Umakoshi, M. Niinomi, H. Nakajima, Peculiar elastic behavior of Ti–Nb–Ta–Zr single crystals, Acta Mater. 56 (2008) 2856–2863, https://doi.org/10.1016/j.actamat.2008.02.017.

[61] Z. Zou, M.K. Dunstan, B. McWilliams, R. Hague, M. Simonelli, Identification of an affordable and printable metastable β Ti alloy with outstanding deformation behaviour for use in laser powder bed fusion, Mater. Sci. Eng. A 902 (2024) 146619, https://doi.org/10.1016/j.msea.2024.146619.